buildings

MDPI

Article

Modified Constitutive Model and Practical Calibration Method for Constructional 7075-T6 Aluminum Alloy

Yishu Zhang [1,2], Lin Zhao [3], Zhenggang Cao [1,2,*] and Bizhao Wu [1,2]

[1] Key Laboratory of Structures Dynamic Behaviour and Control of the Ministry of Education, Harbin Institute of Technology, Harbin 150090, China; 20b933008@stu.hit.edu.cn (Y.Z.); beingw@hit.edu.cn (B.W.)
[2] Key Laboratory of Smart Prevention and Mitigation of Civil Engineering Disasters, Ministry of Industry and Information Technology, Harbin Institute of Technology, Harbin 150090, China
[3] School of Civil Engineering, Heilongjiang University, Harbin 150080, China; 2025003@hlju.edu.cn
* Correspondence: caohit@hit.edu.cn; Tel.: +86-137-6681-9757

Abstract

Recently, high-strength 7075-T6 aluminum alloy has demonstrated promising application prospects in large-span spatial structures given its exceptional mechanical properties. However, the classical Ramberg–Osgood (R–O) constitutive model cannot accurately predict the mechanical behavior of 7075-T6 aluminum alloy in the large-strain stage, compromising the structural reliability of designs. Herein, the full-range stress–strain curves of 7075-T6 aluminum alloy were investigated through tensile tests. Mechanical property indices were obtained, and the classical R–O model was calibrated for 7075-T6 aluminum alloy. Furthermore, an improved R–O model based on piecewise functions was proposed to address the significant prediction errors under large-strain conditions ($\varepsilon > 0.015$). Compared with the classical R–O model, the modified model exhibited a reduction of over 75% in stress–strain curve deviation. Moreover, an approximate value method only based on nonproportional extension strength and elastic modulus was proposed for the calibration of the modified model, considerably enhancing the engineering practicality of the modified constitutive model.

Keywords: 7075-T6 aluminum alloy; tensile test; large-strain behavior; Ramberg–Osgood constitutive model; constitutive model calibration

check for updates

Academic Editor: Mario D'Aniello

Received: 2 June 2025
Revised: 27 June 2025
Accepted: 28 June 2025
Published: 30 June 2025

Citation: Zhang, Y.; Zhao, L.; Cao, Z.; Wu, B. Modified Constitutive Model and Practical Calibration Method for Constructional 7075-T6 Aluminum Alloy. *Buildings* **2025**, *15*, 2306. https://doi.org/10.3390/buildings15132306

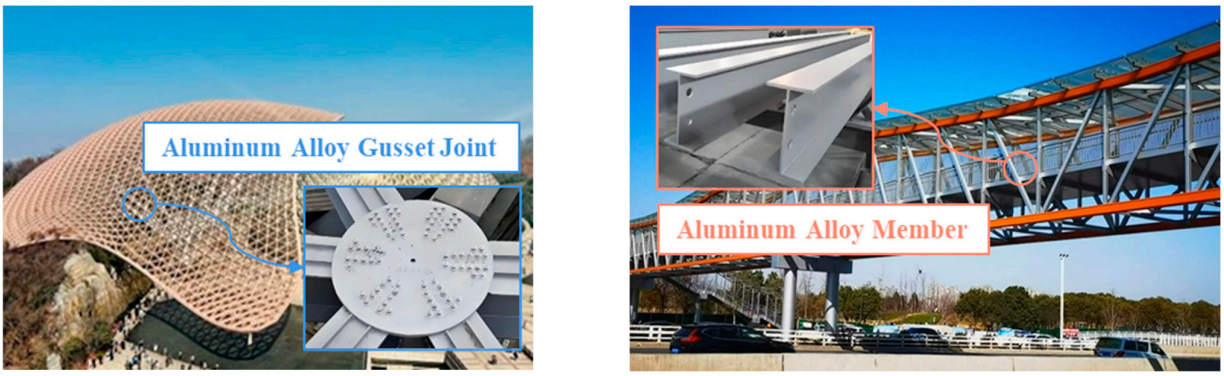
Copyright: © 2025 by the authors. Licensee MDPI, Basel, Switzerland. This article is an open access article distributed under the terms and conditions of the Creative Commons Attribution (CC BY) license (https://creativecommons.org/licenses/by/4.0/).

1. Introduction

Aluminum alloys are characterized by excellent corrosion resistance, low-temperature toughness, and ease of extrusion forming, making them ideal materials for fabricating lightweight construction components and for use in aerospace vehicles, automobiles, and ships. Recently, advancements in smelting technology and extrusion forming equipment have further enhanced their mechanical properties, leading to their widespread application as primary structural materials in civil engineering projects [1,2].

Up to now, 6 series aluminum alloys, such as 6061-T6 and 6082-T6, have been extensively employed in long-span spatial structures [3,4], bridges, and power transmission towers (Figure 1). However, their relatively low strength, with post-heat-treatment nominal yield strengths typically below 350 MPa, limits their application in civil engineering projects, leading to difficulties such as oversized component dimensions due to insufficient material strength. By contrast, 7 series aluminum alloys, particularly 7075 alloy, have extremely high strength, with a tensile strength reaching up to 560 MPa. It is almost twice that of 6061 aluminum alloy and approaching the strength of low-carbon steel. In addition, these

alloys can achieve further strength enhancement through heat treatment and maintain excellent mechanical performance at temperatures below 150 °C. Consequently, 7 series aluminum alloys have recently progressively attracted attention in both academic research and engineering practice.



(**a**) Aluminum alloy latticed shell (**b**) Aluminum alloy pedestrian bridge

Figure 1. Aluminum alloy structure projects.

Accurate characterization of material properties is the critical foundation for advancing the structural applications of 7 series aluminum alloys. In 2011, Zhang et al. [5] and Li et al. [6] experimentally studied the static constitutive relationships of 7A04-T6 aluminum alloy. Wang and Wang [7] performed several monotonic and cyclic loading tests on 7A04-T6 aluminum alloy specimens and established their constitutive behavior under cyclic loading conditions. However, the practical implementation of 7A04-T6 aluminum alloy in long-span structures has been significantly limited because of its deficiencies in microstructural stability and high susceptibility to stress corrosion cracking. Thereafter, the research focus has shifted toward 7075-T6 aluminum alloy given its superior processability. In 2015, Zhang et al. [8] systematically investigated the quasistatic, intermediate strain rate and high strain rate dynamic mechanical properties of high-strength 7075-T6 aluminum alloy. On this basis, the Johnson–Cook constitutive equation was established. Then, Chen et al. [9,10] experimentally and theoretically studied the mechanical properties of 7075-T73 aluminum alloy under repeated fire exposure conditions. They developed empirical models for accurately estimating post-fire residual mechanical properties. In 2017, Senthil et al. [11] conducted standardized and notched round-bar testing of 7075-T6 aluminum alloy, revealing its plastic flow and fracture behaviors under multiaxial stress states, varied strain rates, and temperature gradients. In 2023, Wang et al. [12] proposed and optimized a data-driven deep neural network constitutive model to improve the accuracy of predicting the flow behavior of 7075 aluminum alloy at high temperatures. In 2024, Wu et al. [13] revealed the warm flow characteristics and microstructural evolution features of a solution-treated 7075 aluminum alloy and proposed an elastic-visco-plastic constitutive model to capture the flow stress behavior under warm deformation. In the same year, Xi et al. [14] investigated tension tests on 7075-T6 aluminum alloy at low temperatures ranging from 20 °C to −165 °C and proposed a full-range constitutive model to estimate the stress–strain behaviors of AA 7075-T6. However, the above-mentioned research on the material properties of 7075-T6 aluminum alloy either merely offers a qualitative analysis of the key factors affecting material performance or, despite the proposal of a clear constitutive model, the large number of required parameters significantly restricts its practical applicability. Especially, the existing constitutive models have limited accuracy in simulating material behavior in the large-strain stage, failing to reliably capture the material's limit state.

Therefore, more comprehensive investigations into the constitutive model of constructional 7075-T6 aluminum alloy are imperative, especially in the large-strain stage.

This study mainly focused on the constitutive modeling and calibration of architectural 7075-T6 aluminum alloy. The layout of this paper is as follows. Section 2 presents five tensile tests conducted on 7075-T6 aluminum alloy bar specimens to determine their mechanical properties. Section 3 calibrates the classical Ramberg–Osgood (R–O) constitutive model according to experimental data and critically analyzes its applicability to large-strain regimes. Section 4 introduces a modified R–O model, with a comparative analysis demonstrating its superior performance. Section 5 validates the proposed modified constitutive model through comparisons of load–displacement curves.

2. Tensile Tests of 7075-T6 Aluminum Alloy Specimens

2.1. Test Setup and Procedure

The 7075-T6 aluminum alloy material used in the experiment was manufactured by Dongguan Zhuohui Hardware Products Co., Ltd. Dongguan, China. It contained 0.35% silicon, 0.21% chromium, 1.67% copper, 0.15% iron, 2.45% magnesium, 0.03% manganese, 0.18% titanium, and 6.31% zinc. Except for the zinc content slightly exceeding the specified range (5.1–6.1%) in the Chinese standard "Chemical composition of wrought aluminum and aluminum alloys" (GB/T 3190-2020) [15], the contents of the other elements all met the standard requirements. Tensile tests on 7075-T6 aluminum alloy specimens were conducted at the Analysis and Testing Center of the Harbin Institute of Technology. The experimental setup and specimen dimensions are shown in Figure 2. The Instron-5982 electro-mechanical universal testing machine was used for displacement-controlled loading, and a constant speed of 1.00 mm/min was maintained throughout the testing process. Deformation measurements were obtained using the Instron 2630-112 extensometer manufactured by Instron Corporation located in Boston, MA, USA, configured with a 50 mm gauge length. The specimens were designed following the Chinese standard "Metallic materials—Tensile testing—Part 1: Method of test at room temperature" (GB/T 228.1-2010) [16]. Five standardized round-bar specimens were fabricated through computerized numerical control (CNC) machining. Dimensional measurements were performed on all specimens before the formal testing. The results demonstrated the exceptional precision of CNC manufacturing, with dimensional deviations for critical parameters consistently within ±0.01 mm.

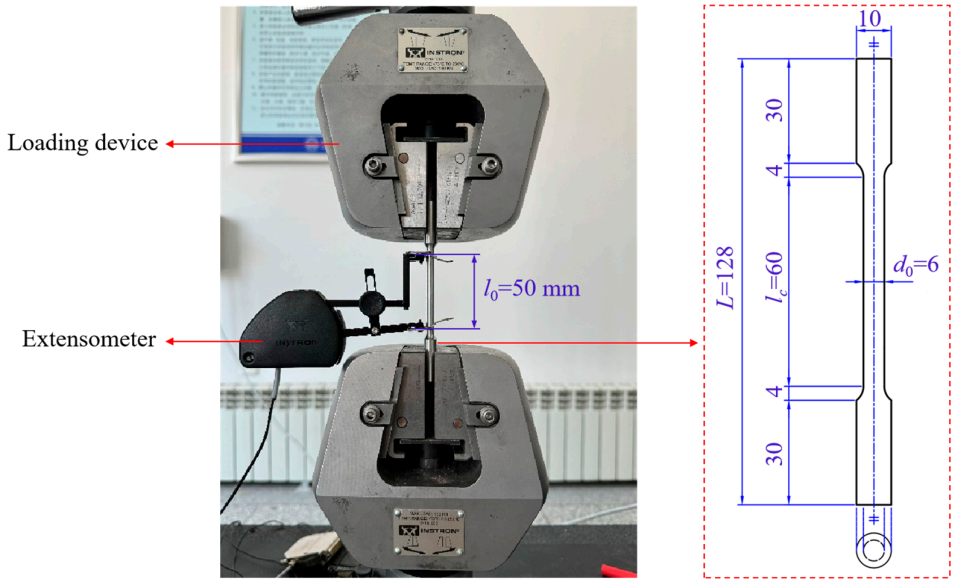


Figure 2. Test setup and specimen dimensions.

2.2. Experimental Phenomena and Results Analysis

2.2.1. Tensile Failure and Engineering Stress–Engineering Strain Curve

Figure 3 illustrates the fracture state of the tested specimens, showing an uneven fracture surface with limited necking phenomena. The specimens showed no visible plastic deformation before the final fracture, which was accompanied by distinct snapping sounds. Figure 4 presents the engineering stress s versus engineering strain e curves of five 7075-T6 aluminum alloy specimens throughout the loading process, which were calculated as follows:

$$s = F/A_0 \tag{1}$$

$$e = \Delta l/l_0 \tag{2}$$

where F is the applied tensile force, with data directly acquired from the Instron-5982 testing machine; A_0 is the initial cross-sectional area in the parallel portion of the tensile specimen, calculated as $A_0 = \pi/4d_0^2$; and Δl is the displacement increment within the gauge length l_0, measured using an extensometer.



Figure 3. Fracture state of the specimens.

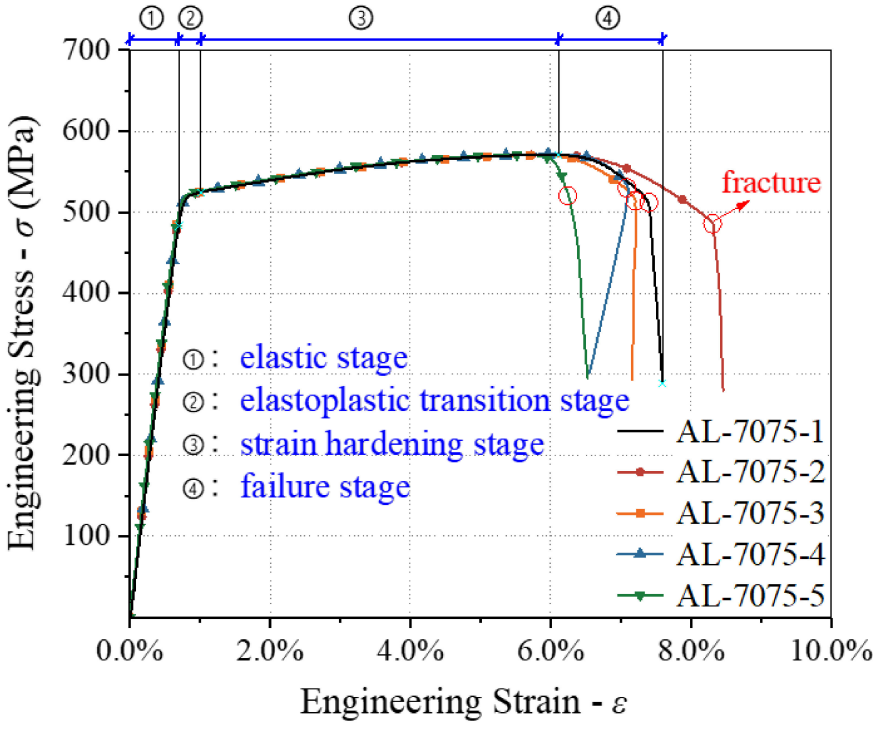


Figure 4. Engineering stress–engineering strain curves.

Figure 4 shows that the five specimens exhibited nearly identical stress–strain curves before necking initiation, indicating the consistency of their material properties and the reliability of the experiments. However, the curves after necking initiation showed a certain degree of dispersion. This could be attributed to two factors: the inherent randomness of the specimen defects and the unexpected measurement errors. Especially for AL-7075-1, AL-7075-2, and AL-7075-3, the necking region in these specimens was just next to the extensometer's grip position. As a result, the necking area could extend beyond the gauge length of the extensometer as it formed and gradually expanded. This led to incomplete deformation measurement after necking, as evidenced by the fact that the fracture strain of the three specimens is lower than that of AL-7075-1 and AL-7075-2 (Figure 4). Furthermore, the occurrence of necking near the grip position may result in sudden and irregular slippage of the extensometer, causing the stress s–strain e curves to drift back in the descending stage, which was more severe in AL-7075-4 compared to AL-7075-3. Nevertheless, the stress s–strain e curves prior to the onset of necking remained unaffected by this phenomenon.

Taking specimen AL-7075-1 as a representative example, the mechanical response can be categorized into four stages based on curve characteristics: ① elastic stage, ② elasto-plastic transition stage, ③ strain hardening stage, and ④ failure stage (Figure 4). In the elastic stage, stress and strain maintain a linear proportional relationship and increase progressively. Subsequently, the specimen enters the elastoplastic transition stage, marked by a distinct inflection point indicating the onset of nonlinear behavior. As the curve's slope decreases sharply to a certain threshold, the specimen transitions into the strain hardening stage, where the stress still increases at a relatively slower rate as the strain increases. Finally, in the failure stage, the stress decreases progressively until the specimen is eventually fractured.

2.2.2. Mechanical Properties of 7075-T6 Aluminum Alloy

To accurately determine the mechanical properties of 7075-T6 aluminum alloy, this section considers the cross-sectional area variations before necking initiation and transforms the s–e curves into the true stress σ–true strain ε curves. The following assumptions were adopted: (1) preservation of constant volume during the elastoplastic deformation of the specimen and (2) uniform strain distribution within the deformed region. The transformation formulas for the true stress σ and the true strain ε are given in Equations (3) and (4), respectively. On this basis, the true stress–true strain curves of the specimens before the necking points were obtained, as shown in Figure 5.

$$\sigma = s(1 + e) \tag{3}$$

$$\varepsilon = \ln(1 + e) \tag{4}$$

Post-necking, extensometer-based strain measurements become invalid because of localized nonuniform deformation. Therefore, the post-necking true stress–true strain curves were unknown. However, the equivalent plastic fracture strain ε_f and the true fracture strength f_f can be estimated according to the cross-sectional area reduction after fracture, expressed in the following equations:

$$\varepsilon_f = \ln\left(\frac{1}{1 - \Psi}\right) \tag{5}$$

$$f_f = s_f\left(\frac{1}{1 - \Psi}\right) \tag{6}$$

where s_f is the engineering stress at fracture. Ψ is the reduction percentage of the cross-sectional area after fracture, calculated as follows:

$$\Psi = \frac{A_0 - A_1}{A_0} = 1 - \frac{A_1}{A_0} = \left(1 - \frac{d_1^2}{d_0^2}\right) \times 100\% \quad (7)$$

where A_0 is the original cross-sectional area within the gauge region, A_1 is the cross-sectional area at the fractured section, d_0 is the original diameter of the parallel portion of the tensile specimen, and d_1 is the diameter at the fractured section of the specimen.

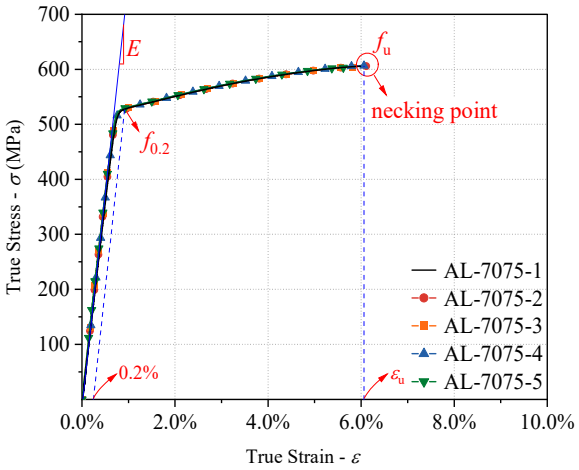


Figure 5. True stress–true strain curves before the necking points.

From the experimental data, the mechanical properties of 7075-T6 aluminum alloy were determined (Table 1). E is the elastic modulus, $f_{0.1}$ is the true stress corresponding to a plastic strain of 0.1% as the proportional limit strength, $f_{0.2}$ is the true stress at a plastic strain of 0.2% as the nonproportional extension strength (yield strength), f_u is the ultimate tensile strength, ε_u is the ultimate strain, and ε_f is the equivalent fracture strain. Considering the average values from the five specimens, the elastic modulus of 7075-T6 aluminum alloy was approximately 74 GPa, the yield strength was 528 MPa, the ultimate tensile strength was 605 MPa, the yield-to-tensile ratio was 0.87, the ultimate strain was 5.9%, and the equivalent fracture strain was 32.8%.

Table 1. Mechanical property indicators of 7075-T6 aluminum alloy.

Specimen Number	E (GPa)	$f_{0.1}$ (MPa)	$f_{0.2}$ (MPa)	f_u (MPa)	f_f (MPa)	ε_u (%)	ε_f (%)	Ψ (%)
AL-7075-1	71.66	524	528	606	729	6.0	36.8	30.8
AL-7075-2	74.55	523	527	606	706	6.1	37.3	31.1
AL-7075-3	75.22	523	527	604	683	5.8	28.6	24.9
AL-7075-4	73.17	525	529	607	752	6.1	36.1	30.3
AL-7075-5	76.02	524	529	603	665	5.6	25.2	22.3

3. Classical R–O Constitutive Model and Calibration

3.1. Power-Law Hardening Constitutive Model

Accurate constitutive relationships are fundamental for analyzing the mechanical behavior of aluminum alloy components. Researchers worldwide have extensively studied these relationships [17,18] and proposed multilinear models, continuous models, and others. Among these, the R–O power-law hardening constitutive model is the representative three-parameter continuous model proposed by Ramberg and Osgood in 1943 [19]. This

model has been recommended by the International Union of Laboratories and Experts in Construction Materials, Systems and Structures for describing the constitutive relationships of materials with continuous stress–strain curves [20]. The R–O model exhibits excellent agreement with actual material behaviors, particularly for aluminum alloys, which has led to its widespread adoption, such as for 6061, 6063, and 6082 aluminum alloys. Its conventional mathematical expression is:

$$\varepsilon = \frac{\sigma}{E} + \varepsilon_0 \left(\frac{\sigma}{f_{\varepsilon_0}} \right)^n \tag{8}$$

where ε_0 is the plastic strain corresponding to the stress reaching the nonproportional extension strength $f_{0.2}$ (0.002), n is the strain hardening exponent characterizing material hardening behavior, and E and $f_{0.2}$ can be determined from the experimentally measured true stress–strain curves (Figure 5). The method refers to the standard for tensile tests of metallic materials at room temperature.

3.2. Constitutive Model Parameter Calculation Methods

There are three primary methods for calculating the strain hardening exponent n of aluminum alloys: the linear least squares (LLS) method, the traditional two-point (TP) method, and the Steinhardt approximate (STE) method.

3.2.1. LLS Method

First, we rearrange Equation (8) and apply a logarithmic transformation to both sides. Then, the nonlinear relationship between the plastic strain ε_p and stress σ in the constitutive model is linearized. Thus, a linear correlation between the variables Y and X is established as follows:

$$Y = nX \tag{9}$$

$$Y = \ln\left(\frac{\varepsilon - \sigma/E}{\varepsilon_0} \right) = \ln\left(\frac{\varepsilon_p}{\varepsilon_0} \right),\ X = \ln\left(\frac{\sigma}{f_{\varepsilon_0}} \right). \tag{10}$$

For a given set of experimentally measured true stress sample data σ_i, logarithmic transformation can be applied to derive the corresponding stress-characterizing sample data X_i, where $X_i = \ln(\sigma_i / f_{\varepsilon_0})$. The strain-characterizing fitted data Y_i can be derived from a linear relationship, expressed as $Y \sim X$, $Y_i = nX_i = n \times \ln(\sigma_i / f_{\varepsilon_0})$. Meanwhile, the measured strain sample data ε_i^{test} corresponding to the stress sample data σ_i can be obtained from the experimental stress–strain relationship, and the strain-characterizing experimental data can be obtained after logarithmic transformation. Then, by minimizing the sum of squared residuals between the measured values Y_i^{test} and the fitted values Y_i as the objective function, the partial derivative of function φ with respect to n is derived according to the least squares theory, as illustrated in Equations (11) and (12). Finally, setting $\partial\varphi/\partial n = 0$ leads to the derivation of the optimal solution for n.

$$\min\varphi = \|r_i\|^2 = \sum_{i=1}^{m} \left(Y_i^{test} - Y_i \right)^2 = \sum_{i=1}^{m} \left(Y_i^{test} - n \cdot X_i \right)^2 \tag{11}$$

$$\partial\varphi/\partial n = 2\left(\sum_{i=1}^{m} nX_i^2 - \sum_{i=1}^{m} X_i Y_i^{test} \right) = 0 \tag{12}$$

where r_i is the residual between each sample data Y_i and Y_i^{test}, and m is the number of sample points.

The formula for calculating the strain hardening index n^{LLS} can be derived by further organizing Equation (12). For aluminum alloy structural members under normal service

conditions or properly designed configurations, deformation typically occurs within the small-strain range during service. Therefore, the experimental data within the common-strain range [0%, 1.5%] were employed for parameter fitting in this study.

$$n^{\mathrm{LLS}} = \sum_{i=1}^{\mathrm{m}} X_i Y_i^{\mathrm{test}} / \sum_{i=1}^{\mathrm{m}} X_i X_i \tag{13}$$

3.2.2. Traditional TP Method

The LLS method yields a constitutive relationship that closely approximates actual material properties. However, it requires extensive experimental data, which is inconvenient for practical engineering applications. Considering that the R–O model passes through a fixed point ($\varepsilon_0 + f_{\varepsilon_0}/E$, f_{ε_0}) and involves one unknown parameter n to be solved, the TP method selects an additional point ($\varepsilon_x + f_{\varepsilon_x}/E$, f_{ε_x}) as the second reference point. By substituting ($\varepsilon_x + f_{\varepsilon_x}/E$, f_{ε_x}) into Equation (8) and simplifying, the calculation formula for n is derived as follows:

$$n = \frac{\ln(\varepsilon_x/\varepsilon_0)}{\ln(f_{\varepsilon_x}/f_{\varepsilon_0})} \tag{14}$$

where ε_x and f_{ε_x} are respectively the plastic strain and the measured stress value at the selected reference point. For aluminum alloys that lack a distinct yield plateau, ε_x is generally taken as 0.001, and the corresponding stress value f_{ε_x} is denoted as $f_{0.1}$. Thus, the formula for calculating n^{TP} in the TP method can be expressed as follows:

$$n^{\mathrm{TP}} = \frac{\ln(1/2)}{\ln(f_{0.1}/f_{0.2})} \tag{15}$$

3.2.3. STE Method

As standards typically only specify a material's elastic modulus and nonproportional extension strength $f_{0.2}$, the applicability of the least squares method and the traditional TP method is limited. To address this, Steinhardt [21] proposed an approximate value method for determining the strain hardening exponent, which relies solely on the material's nonproportional extension strength. This method, which is straightforward and widely validated by numerous experiments, is expressed as follows:

$$n^{\mathrm{STE}} = \frac{f_{0.2}}{10} \tag{16}$$

3.3. Constitutive Model Calibration and Result Analysis

From the classical R–O model and tensile test data from Section 2.2, the strain hardening exponents of 7075-T6 aluminum alloy were calculated using the LLS, TP, and STE methods. The calculated results are summarized in Table 2. The table demonstrates that all three methods exhibited good stability. The same method shows small variations among different tensile specimens. Specifically, the average strain hardening index obtained by the LLS method was 63.16, whereas the TP method yielded 79.75 and the STE method gave 52.81.

Table 2. Strain hardening index n obtained using different methods.

Specimen Number	n^{LLS}	n^{TP}	n^{STE}
AL-7075-1	66.48	77.23	52.83
AL-7075-2	61.43	79.45	52.72
AL-7075-3	62.29	80.54	52.75
AL-7075-4	62.87	86.30	52.88
AL-7075-5	62.71	75.21	52.87

Taking tensile specimen AL-7075-1 as an example, Figure 6 presents the measured stress–strain curve of the specimen and the theoretical stress–strain curves using the LLS, TP, and STE methods. Within the common-strain range (0–1.5%), all three methods effectively captured the stress–strain relationship of the 7075-T6 aluminum alloy. The theoretical models exhibited only minor deviations from the measured values at the curve transition stage, where the theoretical curves slightly lagged behind the actual timing of the material entering the elastoplastic stage. However, in the large-strain range (1.5–6%), all three methods visibly underestimated the strain hardening degree of 7075-T6 aluminum alloy. There was a notable discrepancy between the classical R–O model and the measured stress–strain curve. When the true strain was 6%, the maximum deviation between the stress derived from the constitutive model and the experimental measurement was approximately 8%. Therefore, a modified constitutive model for 7075-T6 aluminum alloy must be further developed to reliably simulate the full-stage mechanical behavior of this alloy.

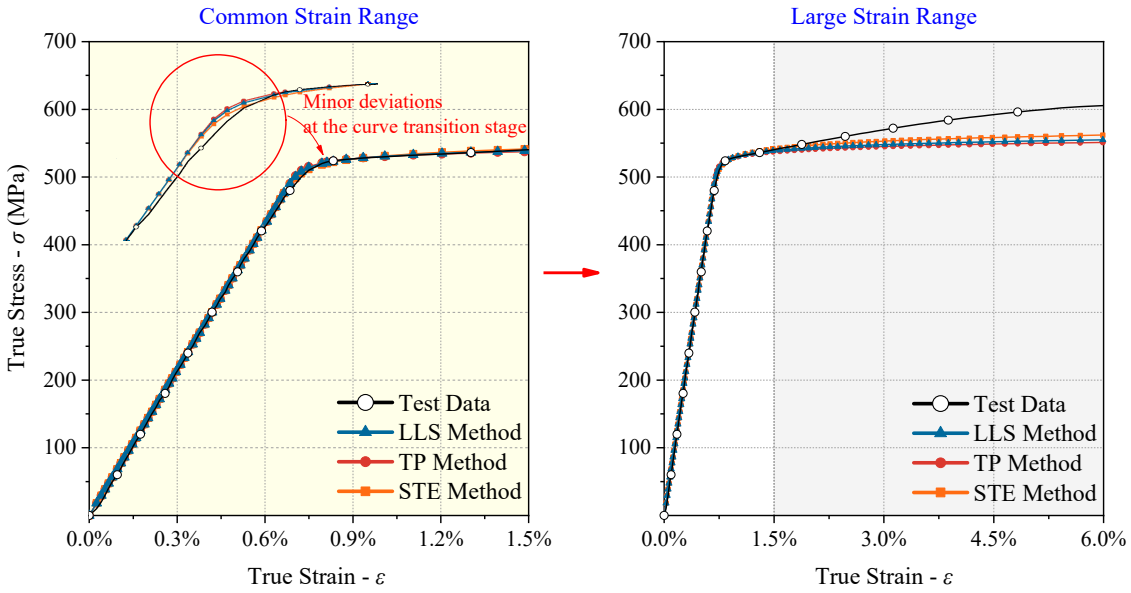


Figure 6. Comparison of the theoretical constitutive relationship and the measured σ–ε curves.

4. Modified R–O Constitutive Model and Calibration

4.1. Piecewise Constitutive Model Establishment

To address the applicability limitations of the classical R–O model, this section proposes a modified piecewise constitutive model with large-strain range corrections, referred to as the modified R–O model. First, the total strain ε is decomposed into two parts: the elastic strain component ε_e and the plastic strain component ε_p. Accordingly, the traditional R–O model described by Equation (8) can be reformulated as follows:

$$\varepsilon_e = \frac{\sigma}{E} \tag{17}$$

$$\varepsilon_p = \varepsilon_0 \left(\frac{\sigma}{f_{\varepsilon_0}} \right)^n \tag{18}$$

Equation (17) indicates a linear relationship between the elastic strain and stress, aligning with the fundamental assumption for metallic materials. Meanwhile, Equation (18) demonstrates a power-law relationship between the plastic strain and stress, reflecting the nonlinear characteristics of metallic materials. To refine the classical R–O model in the large-strain range, Equation (18) can be further rearranged to derive the functional relationship of stress with respect to plastic strain in the classical R–O model:

$$\sigma = f_{\varepsilon_0}\left(\frac{\varepsilon_{\mathrm{p}}}{\varepsilon_0}\right)^{\frac{1}{n}} \tag{19}$$

As analyzed in the previous section, the power-law model in Equation (19) exhibits significant discrepancies when describing the stress–strain relationship of 7075-T6 aluminum alloy in the large-strain range. To accurately capture the strain hardening behavior of this alloy, this study employs a piecewise function to characterize the relationship between plastic strain and stress, as shown in Equation (20). In the small-strain range ($\varepsilon_{\mathrm{p}} \le \varepsilon_p^{\mathrm{s}}$), the stress and plastic strain follow a power-law relationship, whereas this relationship transitions to a quadratic function in the large-strain range ($\varepsilon_p^{\mathrm{s}} \le \varepsilon_{\mathrm{p}} \le \varepsilon_p^{u}$).

$$\begin{cases} \sigma = f_{\varepsilon_0}\left(\frac{\varepsilon_{\mathrm{p}}}{\varepsilon_0}\right)^{\frac{1}{n}} & \left(\varepsilon_{\mathrm{p}} \le \varepsilon_{\mathrm{p}}^{\mathrm{s}}\right) \\ \sigma = k\varepsilon_{\mathrm{p}} + k'{\varepsilon_{\mathrm{p}}}^2 + \mathrm{c} & \left(\varepsilon_{\mathrm{p}}^{\mathrm{s}} \le \varepsilon_{\mathrm{p}} \le \varepsilon_{\mathrm{p}}^{\mathrm{u}}\right) \end{cases}, \tag{20}$$

where, $\varepsilon_p^{\mathrm{s}}$ is the plastic strain at the piecewise point, defined as the plastic strain component corresponding to the upper limit of the common-strain range in this study. To ensure the continuity of the piecewise function given in Equation (20), the stress at the piecewise point must satisfy $f_{\mathrm{s}} = f_{\varepsilon_0}\left(\varepsilon_p^{\mathrm{s}}/\varepsilon_0\right)^{1/\mathrm{n}}$. n is the strain hardening exponent, determined from the experimental stress–strain data within the common-strain range (with the calculation method detailed in Section 3.1). k is the linear term coefficient of the stress–plastic strain function after the piecewise point, referred to as the post-strain hardening coefficient. It is determined from the experimental data in the large-strain range. k' is the quadratic term coefficient of the stress–plastic strain function in the large-strain range. c is the constant term of the stress–plastic strain function.

On the basis of the properties of quadratic functions, the coefficients k' and c can be determined using the post-strain hardening coefficient k, the plastic strain and stress at the piecewise point ($\varepsilon_p^{\mathrm{s}}, f_{\mathrm{s}}$), and the plastic strain and stress at the necking point ($\varepsilon_p^{u}, f_{\mathrm{u}}$):

$$k' = \frac{(f_{\mathrm{u}} - f_{\mathrm{s}}) - k\left(\varepsilon_{\mathrm{p}}^{\mathrm{u}} - \varepsilon_{\mathrm{p}}^{\mathrm{s}}\right)}{\left(\varepsilon_{\mathrm{p}}^{\mathrm{u}}\right)^2 - \left(\varepsilon_{\mathrm{p}}^{\mathrm{s}}\right)^2} \tag{21}$$

$$\mathrm{c} = \left(f_{\mathrm{s}} - k\varepsilon_{\mathrm{p}}^{\mathrm{s}}\right) - \frac{(f_{\mathrm{u}} - f_{\mathrm{s}}) - k\left(\varepsilon_{\mathrm{p}}^{\mathrm{u}} - \varepsilon_{\mathrm{p}}^{\mathrm{s}}\right)}{\left(\varepsilon_{\mathrm{p}}^{\mathrm{u}}/\varepsilon_{\mathrm{p}}^{\mathrm{s}}\right)^2 - 1}. \tag{22}$$

Furthermore, to address the inaccurate stress–strain relationship after the limit point in the experiments, this study employs a linear assumption to extrapolate the material's nonlinear behavior from the onset of necking to fracture. The final complete modified R–O model is presented in Figure 7.

4.2. Modified Constitutive Model Calibration and Result Analysis

4.2.1. LLS Method

The strain hardening exponent n in the proposed modified R–O model (before the piecewise point) could be calculated using the STE method. The plastic strain at the piecewise point was determined from the results shown in Figure 6, which was 1.5% for 7075-T6 aluminum alloy, corresponding to the upper limit of the common-strain range in building applications. The stress at the piecewise point was set as $f_{\mathrm{s}} = f_{0.2}(\varepsilon_p^{\mathrm{s}}/0.002)^{1/\mathrm{n}^{\mathrm{STE}}}$. In the modified model, the experimentally measured ultimate stress f_{u} was adopted (Table 1). The ultimate plastic strain was calculated using $\varepsilon_p^{u} = \varepsilon_{\mathrm{u}} - f_{\mathrm{u}}/E$, where E is the elastic

modulus. For the post-strain hardening coefficient k beyond the piecewise point, the LLS method was used to fit the test data of the tensile specimens. Simultaneously, the quadratic term coefficient k' and the constant term c were derived from Equations (21) and (22). The fitting results for the modified R–O model are summarized in Table 3. According to the constitutive parameters from five tensile specimens, the average ε_p^s at the piecewise point of the modified model was 0.77%, the average ε_p^u at the ultimate point was 5.1%, and the average k was 2624 MPa.

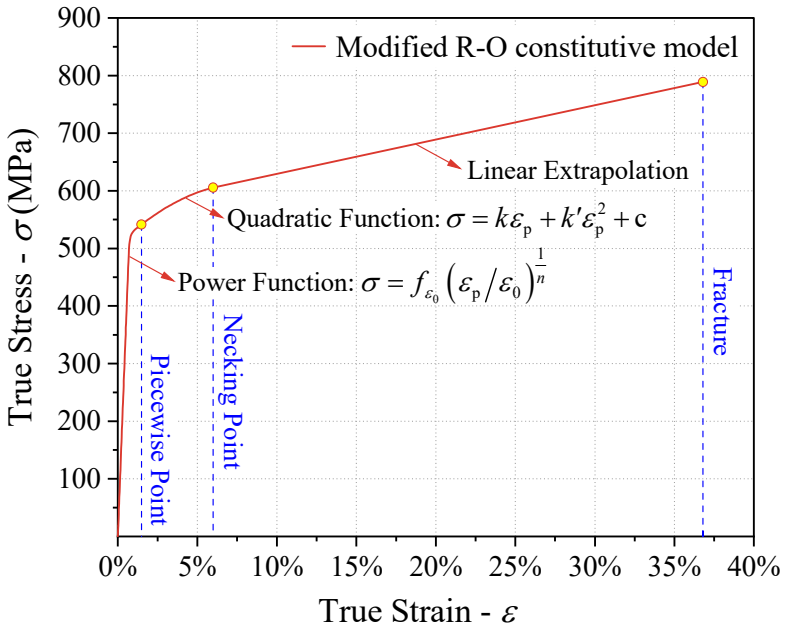


Figure 7. Modified R–O model.

Table 3. Constitutive parameters of the modified R–O model based on the LLS method.

Specimen Number	n	ε_p^s	ε_p^u	f_s (MPa)	f_u (MPa)	k	k'	c
AL-7075-1	52.83	0.0073	0.052	540	606	2597	−18,917	522
AL-7075-2	52.72	0.0076	0.053	540	606	2637	−19,653	521
AL-7075-3	52.75	0.0076	0.050	541	604	2638	−19,773	521
AL-7075-4	52.88	0.0080	0.052	542	607	2612	−19,148	522
AL-7075-5	52.87	0.0081	0.048	542	603	2638	−19,855	522

4.2.2. Approximate Value Method

This study further proposes an approximate value method for determining the parameters of the modified R–O model to enhance practical engineering applicability. The piecewise point of the modified R–O model is assumed as the moment when the elastic strain becomes equal to the plastic strain. By simultaneously solving Equations (17) and (18), the approximate formulas for the piecewise point stress f_s and plastic strain ε_p^s are derived as follows:

$$f_s = \left(\frac{0.002 \cdot E}{{f_{0.2}}^n}\right)^{\frac{1}{1-n}} \tag{23}$$

$$\varepsilon_p^s = \left(\frac{f_{0.2}}{0.002^{\frac{1}{n}} \cdot E}\right)^{\frac{n}{n-1}}, \tag{24}$$

where n is determined using the STE method as $f_{0.2}/10$. That is, ε_p^s and f_s can be calculated only according to the nonproportional extension strength $f_{0.2}$ and the elastic modulus E of 7075-T6 aluminum alloy.

In the proposed approximate value method, k is also calculated just according to the material's nonproportional extension strength $f_{0.2}$. In Equation (25), α represents the proportionality coefficient obtained through fitting (with a value of 5).

$$k = \alpha \cdot f_{0.2}. \tag{25}$$

In the proposed approximate value method, f_u is estimated from the material's yield-to-tensile ratio β and nonproportional extension strength $f_{0.2}$, as shown in Equation (26). The ultimate plastic strain is then estimated using Equation (27). According to the results in Section 2.2, β for 7075-T6 aluminum alloy was 0.87. The proposed Equations (26) and (27) are obtained through the fitting of the experimental data:

$$f_u = \frac{f_{0.2}}{\beta} \tag{26}$$

$$\varepsilon_p^u = \frac{(1+\beta)(f_u - f_s)}{k} + \varepsilon_p^s. \tag{27}$$

Table 4 lists the constitutive parameters derived from the proposed approximate value method. The model exhibited an average ε_p^s of 0.73% at the piecewise point, an average ε_p^u of 5.2% at the ultimate point, and an average k of 2640 MPa.

Table 4. Constitutive parameters of the modified R–O model based on the approximate value method.

Specimen Number	n	ε_p^s	f_s	ε_p^u	f_u	k	k'	c
AL-7075-1	52.83	0.0076	541	0.051	607	2640	−19,100	458
AL-7075-2	52.72	0.0072	540	0.051	606	2635	−19,384	457
AL-7075-3	52.75	0.0072	540	0.051	606	2635	−19,384	457
AL-7075-4	52.88	0.0074	542	0.051	608	2645	−19,371	459
AL-7075-5	52.87	0.0071	542	0.054	608	2645	−20,258	459

4.2.3. Analysis of Calibration Results

Taking specimen AL-7075-1 as an example, Figure 8 compares the stress–strain curves obtained from the modified R–O model, the traditional R–O model, and the experimental measurements. Figure 9 illustrates the residual ratio γ_{error} between the constitutive model and experimental results ($\gamma_{error} = \Delta\sigma/f_{0.2}$). As shown in Figures 8 and 9, the improved R–O model proposed in this study evidently aligned more closely with the experimentally measured stress–strain relationship compared with the classical model. Notably, in the large-strain range, the residual ratio of the classical R–O model even exceeded 8%. The residual ratio between the modified R–O model and experimental values was reduced by approximately 75% relative to the classical model, consistently remaining below 2%. This indicated a significant enhancement in the accuracy of the modified model. Additionally, the residual ratio of the proposed approximate value method was only slightly higher than that of the LLS method, validating the effectiveness of the approximation approach.

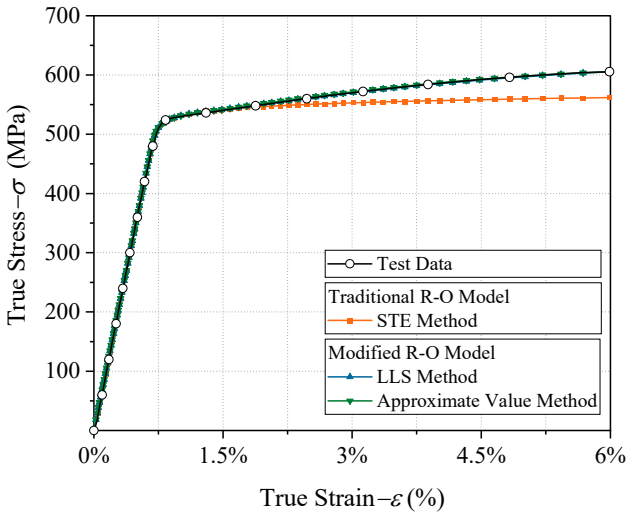


Figure 8. Stress–strain curves of the constitutive model and the experimental measurements (AL-7075-1).

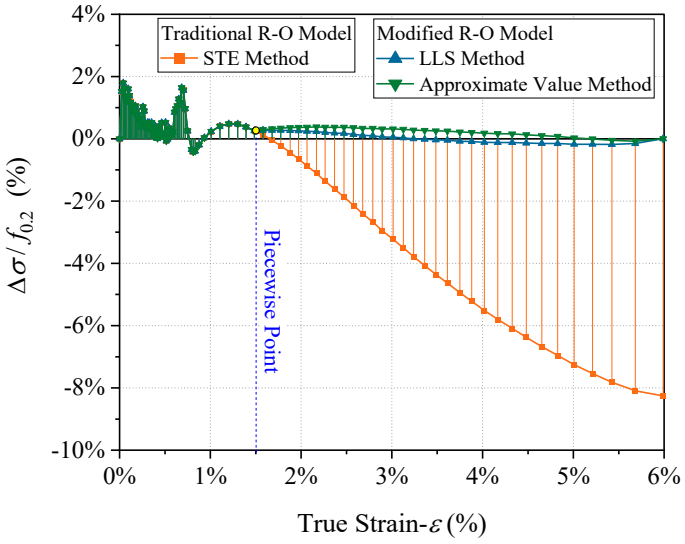


Figure 9. Residual ratio between the constitutive model and the experimental measurements (AL-7075-1).

5. Verification of the Modified R–O Constitutive Model

To further validate the accuracy of the modified R–O model, this section establishes a refined finite element model of the AL-7075-1 tensile specimen using ABAQUS finite element software Ver.2024 (Figure 10). The C3D8R element type was employed to simulate nonlinear mechanical behavior, which has good deformation and stress analysis capabilities. The model is divided into 8928 elements, with an approximately mesh size of 1 mm. There are 8 layers of elements in the radial direction of the parallel portion section. Both the classical R–O and modified R–O models are employed to determine the material's constitutive relationships. Reference points are established at the centers of the cross-sections located at both ends of the model. These reference points are coupled to the displacements of the specimen clamping ends and serve as the nodes through which boundary conditions are applied. The boundary conditions are defined as a fixed constraint at one end of the specimen and an axial displacement load applied to the other end.

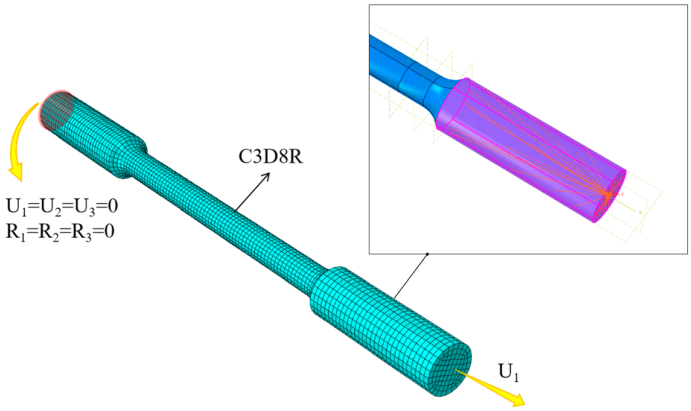


Figure 10. Finite element model of tensile specimen AL-7075-1.

Figure 11 compares the simulated load–displacement curves with the experimental measurements for the tensile specimen. Compared with the classical R–O model, the simulation based on the modified model more accurately captured the nonlinear behavior of 7075-T6 aluminum alloy in the large-deformation range. Furthermore, irrespective of whether the LLS method or the approximation method was used, the simulation results based on the modified constitutive model exhibited small deviations from the experimental measurements before the material reached its ultimate state. When the material's plastic strain reached the ultimate plastic strain, the maximum stress in the simulation based on the modified constitutive model was observed at the central part of the specimen. Then, as the load continued to increase, a necking area formed at the central part of the specimen where the stress was the maximum (Figure 12). The corresponding simulated peak loads were 15.85 kN using the LLS method and 15.99 kN using the approximate value method. Comparing these values with the experimentally measured peak load of 16.13 kN, the simulated results demonstrated errors within 2%, validating the accuracy of the proposed modified model and parameter estimation methods.

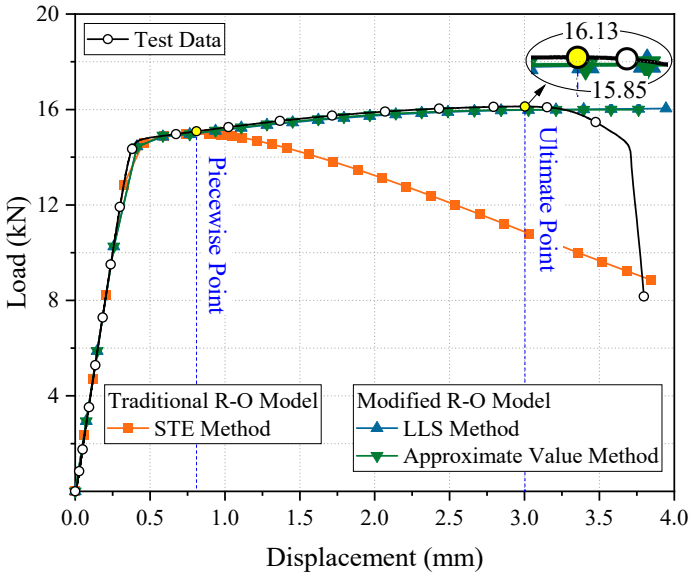
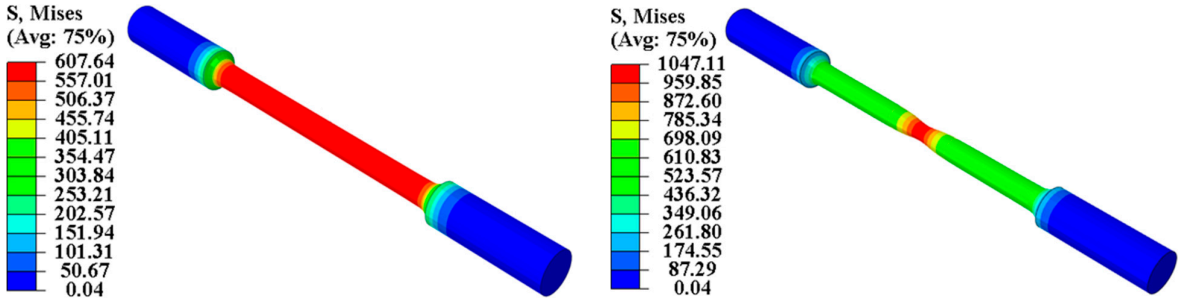


Figure 11. Load–displacement curves of the tensile specimen.



(**a**) The ultimate point (**b**) After necking

Figure 12. Stress distribution cloud diagram.

6. Conclusions

This study systematically investigated the mechanical properties and constitutive relationship characterization of 7075-T6 aluminum alloy through room-temperature tensile tests, mathematical modeling, and numerical simulations. Its main conclusions are as follows:

(1) Room-temperature tensile tests were conducted on 7075-T6 aluminum alloy specimens, obtaining fundamental mechanical properties such as the elastic modulus, nonproportional extension strength, ultimate strength, and fracture stress. These were used to establish an experimental foundation for the proposal and calibration of subsequent constitutive models.

(2) The parameters of the classical R–O constitutive model were calibrated using the LLS method, the traditional TP method, and the STE method. The results indicated that in the common-strain range of 7075-T6 aluminum alloy ($\varepsilon < 0.015$), the reasonable value for n is 50 to 80.

(3) To address the insufficient prediction accuracy of the classical R–O model in the large-strain stage ($\varepsilon > 0.15$), a modified R–O constitutive model based on a piecewise function was proposed. Compared with the classical model, the modified model reduced the fitting error by over 75% across the entire strain range, thereby verifying its effectiveness.

(4) An approximate value method was developed to determine the parameters of the modified R–O model, requiring only the nonproportional extension strength and elastic modulus to achieve rapid model calibration. This approach eliminates the dependency of fitting-based calibration methods on full-range strain data, significantly improving its convenience for engineering applications.

This study provides theoretical and test data support for the mechanical characterization and engineering modeling of 7075-T6 aluminum alloy. The proposed modified constitutive model and parameter calibration method exhibit significant practical value for the structural design and performance prediction of high-strength aluminum alloys.

Author Contributions: Y.Z.: Data curation, Investigation, Software, Writing—original draft, Writing—review & editing. L.Z.: Formal Analysis, Methodology, Software, Validation, Writing—original draft. Z.C.: Conceptualization, Funding acquisition, Resources, Supervision, Writing—review & editing. B.W.: Investigation. All authors have read and agreed to the published version of the manuscript.

Funding: This research was funded by the Chinese National Natural Science Foundation grant number 52278167. The APC was funded by the Chinese National Natural Science Foundation grant number 52278167.

Data Availability Statement: Data that support the findings of this study may be made available upon reasonable request.

Acknowledgments: This work was conducted with financial support from the Chinese National Natural Science Foundation (project designation: 52278167). All authors have read and agreed to the published version of the manuscript.

Conflicts of Interest: The authors declare that they have no known competing financial interests or personal relationships that could have appeared to influence the work reported in this paper.

Abbreviations

The following abbreviations are used in this manuscript:

CNC	computerized numerical control
LLS	linear least squares
TP	two point

References

1. Mazzolani, F.M. *Aluminium Alloy Structures*, 2nd ed.; Chapman & Hall: London, UK, 1995.
2. Kissell, R.J.; Ferry, R.L. *Aluminum Structures: A Guide to Their Specifications and Design*, 2nd ed.; John Wiley & Sons: New York, NY, USA, 2002.
3. Xiong, Z.; Guo, X.; Luo, Y.; Zhu, S. Elasto-plastic stability of single-layer reticulated shells with aluminium alloy gusset joints. *Thin-Walled Struct.* **2017**, *115*, 163–175. [CrossRef]
4. Zhao, C.Q.; Zhou, Y.W.; Wang, G.; Li, H.; Wang, Y. Calculation method of the bearing capacity of a novel modular joint of an aluminium alloy lattice shell structure. *Structures* **2021**, *34*, 3268–3282. [CrossRef]
5. Zhang, W.; Xiao, X.K.; Wei, G. Constitutive relationship and failure model of 7A04 aluminum alloys. *Explos. Shock Wave* **2011**, *31*, 81–87. (In Chinese)
6. Li, J.J.; Ding, Y.J.; Wang, C.X.; Li, Z.Y.; Rong, B.; Wan, W.Y. Research on properties test and constitutive model of 7A04-T6 aluminum alloy tubes. *Steel Constr. (Chin. Engl.)* **2019**, *34*, 35–39. (In Chinese)
7. Wang, Y.Q.; Wang, Z.X. Experimental investigation and FE analysis on constitutive relationship of high strength aluminum alloy under cyclic loading. *Adv. Mater. Sci. Eng.* **2016**, 1–16. [CrossRef]
8. Zhang, D.N.; Shangguan, Q.Q.; Xie, C.J.; Liu, F. A modified Johnson-Cook model of dynamic tensile behaviors for 7075-T6 aluminum alloy. *J. Alloys Compd.* **2015**, *619*, 186–194. [CrossRef]
9. Chen, Z.H.; Lu, J.; Liu, H.B. Experimental investigation on mechanical properties of structural aluminum alloys after single and multiple fire exposure. *J. Build Struc.* **2017**, *38*, 149–159+174. (In Chinese)
10. Chen, Z.H.; Lu, J.; Liu, H.B.; Liao, X.W. Experimental investigation on the post-fire mechanical properties of structural aluminum alloys 6061-T6 and 7075-T73. *Thin-Walled Struct.* **2016**, *106*, 187–200. [CrossRef]
11. Senthil, K.; Iqbal, M.A.; Chandel, P.S.; Gupta, N. Study of the constitutive behavior of 7075-T651 aluminum alloy. *Int. J. Impact Eng.* **2017**, *108*, 171190. [CrossRef]
12. Wang, G.; Zhang, P.; Kou, L.Y.; Wu, Y.; Wen, T.; Shang, X.; Liu, Z. Research on constitutive model of aluminum alloy 7075 thermal deformation based on deep neural network. *J. Mech. Sci. Technol.* **2023**, *37*, 707–717. [CrossRef]
13. Wu, J.F.; He, D.G.; Lin, Y.; Chen, Z.J.; Ding, H.B.; Qiu, Y.L. A unified constitutive model and microstructure evolution of a solution treated 7075 aluminum alloys under warm forming condition. *J. Mater. Res. Technol.* **2024**, *30*, 4159–4168. [CrossRef]
14. Xi, R.; Xie, J.; Yan, J.B. Low-Temperature Mechanical Properties of AA 6063-T6 and 7075-T6: Tests and Full-Range Constitutive Models. *J. Mater. Civil Eng.* **2024**, *36*, 04024341. [CrossRef]
15. *GB/T 3190-2020*; Chemical Composition of Wrought Aluminum and Aluminum Alloys. Standards Press of China: Beijing, China, 2020. (In Chinese)
16. *GB/T 228.1-2011*; Metallic Materials-Tensile Testing-Part 1: Method of Test at Room Temperature. Standards Press of China: Beijing, China, 2011. (In Chinese)
17. Baehre, R. *Trycktastravorav Elastoplastikt Material-Nagrafragestallningar (Comparison Between Structural Behaviour of Elastoplastic Materials)*; Rep. No. 16 Tekn.; De Arne Johnson Ingenjorsbyra: Stockholm, Sweden, 1966. (In German)
18. Mazzolani, F.M. Characterization of the s-e law and buckling of aluminum columns. *Constr. Met.* **1972**, *3*, 112–122.
19. Ramberg, W.; Osgood, W.R. *Description of Stress-Strain Curves by Three Parameters*; Technical Note No. 902; National Advisory Committee for Aeronautics: Washington, DC, USA, 1943.

20. DeMartino, A.; Landolfo, R.; Mazzolani, F.M. The use of the Ramberg-Osgood law for materials of round-house type. *Mater. Struct.* **1990**, *23*, 59–67. [CrossRef]
21. Steinhardt, O. Aluminum im Konstruktiven Ingenierbau (Aluminum constructions in civil engineering). *Aluminum* **1971**, *47*, 131–139.

Disclaimer/Publisher's Note: The statements, opinions and data contained in all publications are solely those of the individual author(s) and contributor(s) and not of MDPI and/or the editor(s). MDPI and/or the editor(s) disclaim responsibility for any injury to people or property resulting from any ideas, methods, instructions or products referred to in the content.